Magnetic phase diagram of (Mo 2/3 RE 1/3) 2 AlC, RE = Tb and Dy, studied by magnetization, specific heat, and neutron diffraction analysis

Quanzheng Tao, Maxime Barbier, Aurelija Mockute, Clemens Ritter, Ruslan Salikhov, Ulf Wiedwald, Stuart Calder, Christine Opagiste, Rose-Marie Galera, Michael Farle, et al.

Journal of Physics:
Condensed Matter

PAPER • **OPEN ACCESS**

Magnetic phase diagram of $(Mo_{2/3}RE_{1/3})_2AlC$, RE = Tb and Dy, studied by magnetization, specific heat, and neutron diffraction analysis

To cite this article: Quanzheng Tao *et al* 2022 *J. Phys.: Condens. Matter* **34** 215801

OPEN ACCESS
IOP Publishing
Journal of Physics: Condensed Matter
J. Phys.: Condens. Matter **34** (2022) 215801 (8pp)
https://doi.org/10.1088/1361-648X/ac5bcf

Magnetic phase diagram of $(Mo_{2/3}RE_{1/3})_2AlC$, RE = Tb and Dy, studied by magnetization, specific heat, and neutron diffraction analysis

Quanzheng Tao[1,*], Maxime Barbier[2,3], Aurelija Mockute[1,4], Clemens Ritter[5], Ruslan Salikhov[6], Ulf Wiedwald[6], Stuart Calder[4], Christine Opagiste[7], Rose-Marie Galera[7], Michael Farle[6], Thierry Ouisse[2] and Johanna Rosen[1,*]

[1] Materials Design Division, Department of Physics, Chemistry, and Biology (IFM), Linköping University, SE-581 83 Linköping, Sweden
[2] Uni. Grenoble Alpes, CNRS, Grenoble INP, LMGP, F-38000 Grenoble, France
[3] European Synchrotron Radiation Facility (ESRF), CS 40220, F-38043 Grenoble Cedex 9, France
[4] Neutron Scattering Division, Oak Ridge National Laboratory Oak Ridge, TN 37831, United States of America
[5] Institut Laue-Langevin, BP 156, 38042 Grenoble Cedex 9, France
[6] Faculty of Physics and Center for Nanointegration (CENIDE), University of Duisburg-Essen, 47057 Duisburg, Germany
[7] Institut Neel, CNRS, Univ. Grenoble Alpes, Grenoble INP, FR-38000 Grenoble, France

E-mail: quanzheng.tao@liu.se

Received 24 January 2022, revised 4 March 2022
Accepted for publication 8 March 2022
Published 29 March 2022

Abstract

We report the results of magnetization, heat capacity, and neutron diffraction measurements on $(Mo_{2/3}RE_{1/3})_2AlC$ with RE = Dy and Tb. Temperature and field-dependent magnetization as well as heat capacity were measured on a powder sample and on a single crystal allowing the construction of the magnetic field-temperature phase diagram. To study the magnetic structure of each magnetic phase, we applied neutron diffraction in a magnetic field up to 6 T. For $(Mo_{2/3}Dy_{1/3})_2AlC$ in zero field, a spin density wave is stabilized at 16 K, with antiferromagnetic ordering at 13 K. Furthermore, we identify the coexistence of ferromagnetic and antiferromagnetic phases induced by magnetic fields for both RE = Tb and Dy. The origin of the field induced phases is resulting from the competing ferromagnetic and antiferromagnetic interactions.

Keywords: MAX phase, neutron diffraction, magnetic material

(Some figures may appear in colour only in the online journal)

* Authors to whom any correspondence should be addressed.

1. Introduction

MAX phases, a family of layered transition metal carbides and nitrides, crystalize in a hexagonal structure with $P6_3/mmc$ symmetry, and combine the characteristics of metals and ceramics [1]. This family comprises more than 150 compounds, including alloys, with the general formula $M_{n+1}AX_n$, where M is a transition metal, A is an element from group 12 to 16, and X is either carbon or nitrogen. The abundant chemistry of these materials renders them promising for applications ranging from structural materials at extreme conditions [2], ohmic contact materials for semiconductors [3], and as precursors for their 2D counterparts, MXenes [4, 5].

In 2017, 2D magnetic materials (monolayers of $Cr_2Ge_2Te_6$ and CrI_3) were discovered, displaying layer-dependent magnetic characteristics [6, 7]. Correspondingly, the exploration of magnetism in MAX phases or in two-dimensional magnetic MXene derivatives may lead to their potential applications in spintronics. In 2013, the first magnetic MAX phase, $(Cr_{0.75}Mn_{0.25})_2GeC$, was synthesized by introducing Mn into the known Cr_2GeC MAX phase [8]. This was followed by several Cr and Mn based magnetic MAX phases, including Mn_2GaC [9, 10]. The magnetic properties of these MAX phases are summarized in a review by Ingason *et al* [11]. At that time, the magnetic elements that could be incorporated into the MAX phase structure were, however, still limited.

Since 2017, we have expanded the MAX phase family and their attenable properties through exploration of their quaternary counterparts. We introduced chemical ordering in so called *i*-MAX phases of the general formula of $(M^1_{2/3}M^2_{1/3})_2AC$, where the M elements are in-plane ordered [12]. This discovery has greatly expanded the diversity of M elements and their combinations that can be incorporated into a MAX phase. The first *i*-MAX phases were $(Mo_{2/3}Sc_{1/3})_2AlC$, $(Mo_{2/3}Y_{1/3})_2AlC$, and $(W_{2/3}Sc_{1/3})_2AlC$, showing great promise for 2D materials preparation [12–14]. Furthermore, we introduced rare earth (RE) elements, Ce, Pr, Nd, Sm, Gd, Tb, Dy, Ho, Er, Tm, and Lu, into the family of *i*-MAX phases, forming a class of magnetic *i*-MAX phases of the general formula $(Mo_{2/3}RE_{1/3})_2AlC$ [15, 16]. This class has been further expanded by corresponding phases where the A-element is Ga [17], though the study of magnetization of the latter materials has just been initiated. Recently, the W based $(W_{2/3}RE_{1/3})_2AlC$ has also been synthesized [18]. In the crystal structure of $(Mo_{2/3}RE_{1/3})_2AlC$, bilayers of a quasi-2D magnetic frustrated triangular RE lattice overlay a Mo honeycomb arrangement and an Al Kagomé lattice. A schematic of the crystal structure is shown in figure 1. These magnetic *i*-MAX phases materials show a complex magnetic behavior. In particular, $(Mo_{2/3}Tb_{1/3})_2AlC$ and $(Mo_{2/3}Dy_{1/3})_2AlC$ may have a rich magnetic phase diagram, indicated from our previously reported initial analysis of the magnetization, specific heat and the zero field structures of $(Mo_{2/3}Tb_{1/3})_2AlC$ [15]. Both $(Mo_{2/3}Tb_{1/3})_2AlC$ and $(Mo_{2/3}Dy_{1/3})_2AlC$ show successive magnetic phase transition and magnetization plateaus, indicating the existence of competing interactions [19, 20]. The magnetic structure of these phases has also been studied by muon spin rotation and neutron diffraction, and the $(Mo_{2/3}RE_{1/3})_2AlC$ with RE elements are suggested to be short ranged ordered with strong spin fluctuation [21]. Until now, however, the magnetic field induced phases have not been studied at all. Here, we investigate the field induced phases of $(Mo_{2/3}Tb_{1/3})_2AlC$ and $(Mo_{2/3}Dy_{1/3})_2AlC$ using magnetization, specific heat, and neutron diffraction analysis, to improve the fundamental understanding of these atomically laminated magnetic materials.

2. Experiment

Polycrystalline $(Mo_{2/3}RE_{1/3})_2AlC$ samples were synthesized by solid state reaction of elemental powders of graphite (99.999%), Mo (99.99%) from Sigma-Aldrich, and Al (99.8%) from Alfa Aesar, and RE (99.9%) from Stanford Advanced Materials. Stoichiometric amounts of the elemental powders were heated, at 5 °C per minute, up to 1500 °C and held at 1500 °C for 10 h, before cooling the furnace to room temperature. The loosely sintered powders were crushed into a fine powder that was directly used for further analysis.

$(Mo_{2/3}Dy_{1/3})_2AlC$ single crystals were grown using the solution growth technique in an induction-heated growth reactor that is similar to that already described in reference [22]. RE ingots, Al pellets and Mo powder were placed in a sealed graphite crucible, with typical initial elemental ratios before carbon incorporation Mo:Dy:Al equal to 0.1:0.7:0.2. After applying a maximum temperature of 1800 °C for 1 or 2 h, the growth reactor was slowly cooled down to 1000 °C over 5 to 7 days. The source of C is the graphite crucible walls, and typical C concentrations in the flux may range from $x_C = 0.2$–0.4, as estimated from weighting the crucible before and after growth. After growth, single crystals were extracted from the solidified flux by oxidizing the latter inside a chamber equipped with an air flux bubbling in water. Each growth resulted in hundreds of small single crystals with a wide size distribution and a maximum lateral crystal size up to a few millimeters.

Bulk magnetization measurements on $(Mo_{2/3}Dy_{1/3})_2AlC$ single crystal were conducted using a commercial quantum design MPMS magnetometer. The magnetic field, H, was aligned along the a, b (in plane) and c^* (normal to the a–b planes) crystal axes of a millimeter-sized single crystal of 3.17 mg. Quantitative measurements were performed in the 2–300 K temperature range, with H going up to 7 T. For the powder samples magnetization measurement were carried out with magnetic fields going up to 9 T.

Specific heat measurements (c_p) were measured using the relaxation method with a quantum design PPMS in the 2–300 K temperature range and under magnetic fields up to 9 T. The transition temperature was deduced from the inflexion point for each lambda anomaly.

Neutron powder diffraction (NPD) measurements of $(Mo_{2/3}Tb_{1/3})_2AlC$ and $(Mo_{2/3}Dy_{1/3})_2AlC$ in high field were carried out using the HB-2A high-flux powder diffractometer at the High Flux Isotope Reactor at Oak Ridge National Laboratory. A 5 g powder sample of $(Mo_{2/3}Tb_{1/3})_2AlC$ was pressed into a pellet and loaded in an aluminum cylindrical sample holder. Due to the large neutron absorption of

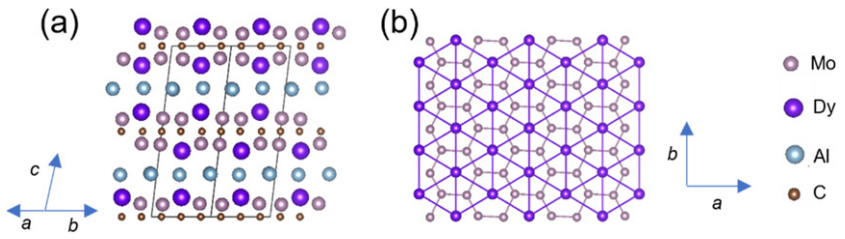

Figure 1. Schematic crystal structure of $(Mo_{2/3}Tb_{1/3})_2AlC$. (a) 3D perspective side view of the *C*2/*c* structure, with (b) corresponding top view of a building block, $(Mo_{2/3}RE_{1/3})_2C$ layer.

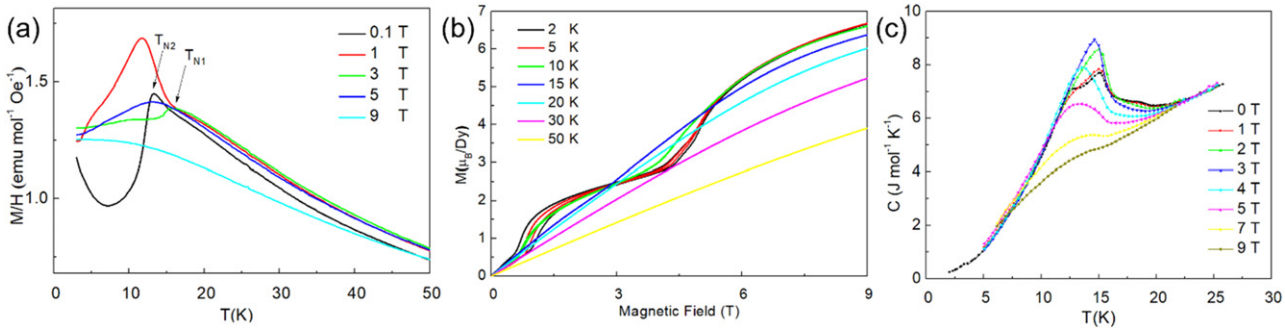

Figure 2. Properties of a $(Mo_{2/3}Dy_{1/3})_2AlC$ powder sample. (a) Magnetic susceptibility (M/H) in different magnetic fields. (b) Magnetization vs magnetic field at different temperatures. (c) Specific heat (c_p) in different magnetic fields.

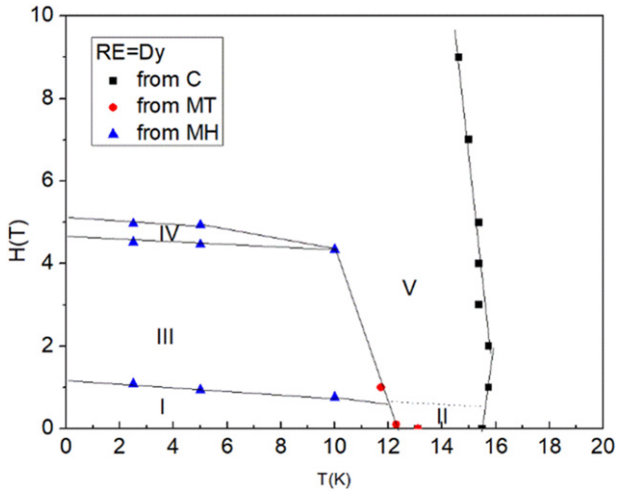

Figure 3. Magnetic phase diagram of $(Mo_{2/3}Dy_{1/3})_2AlC$ obtained from a powder sample.

$(Mo_{2/3}Dy_{1/3})_2AlC$, it was diluted with Flourinert liquid and loaded in an aluminum cylindrical sample holder.

Measurements were performed with a $\lambda = 2.41$ Å neutron wavelength produced by (113) reflections from a vertically focusing Ge monochromator. The data was collected using a ^{3}He detector bank covering a 2θ range of 7°–133° in steps of 0.05°.

High flux NPD measurements of $(Mo_{2/3}Dy_{1/3})_2AlC$ were performed using the D20 diffractometer at the Institut Laue-Langevin. About 1g powdered sample of $(Mo_{2/3}Dy_{1/3})_2AlC$ was loaded in a vanadium sample holder. Measurements were performed at $\lambda = 2.41$ Å.

The magnetic structures were determined by fitting the additional peaks appearing below the ordering temperature by a Gaussian function, to determine the peak position, corrected for zero-offset. The propagation vector was then searched using Fullprof *k-search*, while the symmetry analysis was performed by the Fullprof *BasIreps* [23]. Finally, the magnetic configuration was determined by considering all possible magnetic models that are allowed by symmetry.

3. Results

Figure 2 shows the bulk magnetization and specific heat measurements carried out on a powder sample of $(Mo_{2/3}Dy_{1/3})_2AlC$. Figure 2(a) shows the magnetization versus temperature curve of $(Mo_{2/3}Dy_{1/3})_2AlC$ in different applied magnetic fields. A clear transition can be seen at 13 K, which is marked as T_{N2}. Another faint anomaly can be seen at 16 K marked as T_{N1}. Figure 2(b) shows the magnetization versus field at different temperatures. The magnetization at low temperature shows a magnetization plateau between 1 T and 4.5 T, and another magnetization jump at 5 T. There is hysteresis in both field induced transitions. Figure 2(c) shows the temperature dependence of c_p in different applied magnetic fields from 0 T up to 9 T. In zero field, two lambda anomalies are observed at 16 and 13 K. They correspond to the two magnetic transitions observed at T_{N1} and T_{N2} shown in figure 2(a). A small, not well defined, anomaly, can be seen near 19 K. Its origin is not clear to us, as this was only detected for the powder samples.

The data from the heat capacity measurements shown in figure 2(c) is fully consistent with the observations for the magnetization in figure 2(a). The results are summarized in a phase

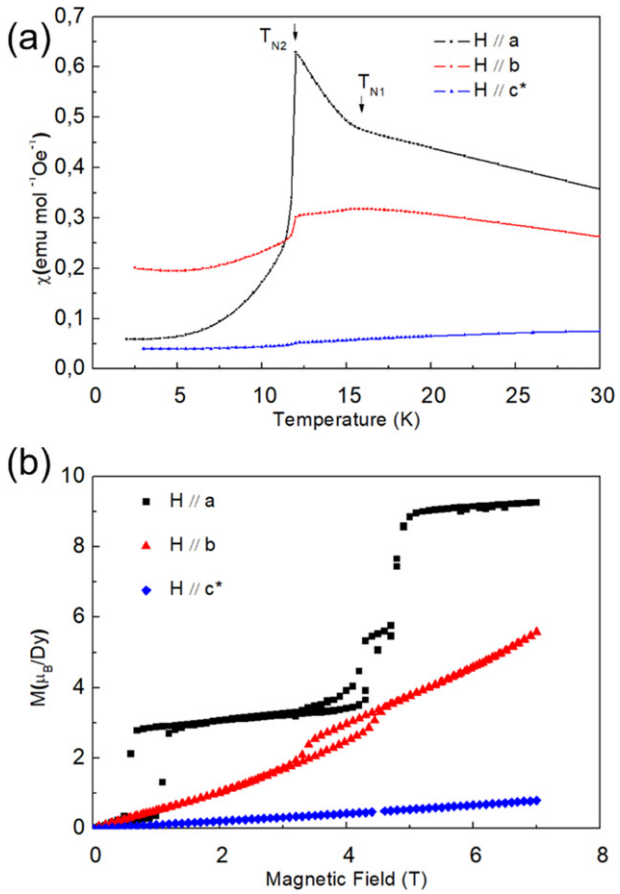

Figure 4. Analysis of a $(Mo_{2/3}Dy_{1/3})_2AlC$ single crystal. (a) Magnetic susceptibility vs temperature for H applied along *a*, *b*, and *c*∗. The applied magnetic field is 0.1 T. (b) Magnetization vs applied magnetic field at 2 K.

diagram as shown in figure 3. For an improved understanding of the behavior under field and as a function of temperature, the study was continued on single crystals.

Figure 4(a) show the magnetization vs temperature along the crystal *a*, *b*, and c^* direction. The *a* and *b* direction are indicated in the schematic in figure 1(b), while the c^* direction is perpendicular to the *a*–*b* plane. The *a* and *b* direction of the crystal are determined with XRD pole figures, and c^* is apparent for thin plate like crystal. The $M(T)$ data along *a* and *b* show the two transitions clearly. Along c^*, on the other hand, only the lowest temperature transition can be seen. The data above 100 K are well fitted to the Curie–Weiss (C–W) law $\chi = C/(T - \theta)$, where *C* is the Curie constant, and θ is the C–W temperature, yielding for *a*, *b*, and c^* directions value of $\theta =$ 16.2 K, 4.7 K, and −64.8 K, respectively. It indicates that a competing ferro and antiferromagnetic correlations, where the ferromagnetic interaction dominates within the *a*–*b* plane and antiferromagnetic interaction dominates between the layers. By comparing the obtained θ to the magnetic ordering temperature $T = 16$ K, we suggest that this material is moderately frustrated. Figure 4(b) shows the magnetization vs applied magnetic field, $M(H)$, along *a*, *b*, and c^*. The 2 K data along the *a*-axis show the AFM order at low field, followed by a metamagnetic transition at about 1 T where the magnetization increases in a first step to around 3.1 μ_B per Dy^{3+}. A second step at about 4 T leads to a further increase to about 9.2 μ_B per Dy^{3+}. Along the *b* axis, there is a single metamagnetic transition indicated at around 4 T. Along c^*, the magnetization increases linearly with no sign of a transition.

4. Magnetic structure of $(Mo_{2/3}Dy_{1/3})_2AlC$ in zero field

We applied neutron diffraction in a magnetic field to study the various magnetic phases as shown in figure 4(a). Figure 5(a) shows the magnetic scattering at 1.5 K, corresponding to phase I. The peaks can be indexed with $\boldsymbol{k} = (0, 0.5, 0)$. The propagation vector is the same as the one found previously for $(Mo_{2/3}Tb_{1/3})_2AlC$ [15]. We did symmetry analysis for this type of $\boldsymbol{k}$ vector within the *C*2/*c* space group. The four Dy atoms split into two orbits and there are two magnetic representations Γ_1 and Γ_2. The detailed symmetry analysis is provided in table 1 of the appendix. By considering all possible magnetic models compatible with this symmetry, the best solution is found by considering basis vectors φ_1 and φ_3 of Γ_2 with a magnetic *R*-factor of 12.7%. It is worth noting that we added a phase factor of $\pi/4$ between the two orbits to ensure an equal size of the magnetic moment for all Dy atoms.

Figure 5(b) shows the magnetic scattering at 14 K, the temperature corresponding to phase II in figure 4(a). The peaks can be indexed with $\boldsymbol{k} = (0, 0.617, 0)$. Similarly, after considering all possible models, the best solution is again provided by considering φ_1 and φ_3 of Γ_2 with a magnetic *R*-factor of 10.7%. Together with reference [15], we have at this point established the zero field magnetic structure for both $(Mo_{2/3}Tb_{1/3})_2AlC$ and $(Mo_{2/3}Dy_{1/3})_2AlC$. In the next sections, we turn to the magnetic structures at high field, corresponding to phase III and phase IV in figure 4(a).

4.1. Field induced magnetic structure of $(Mo_{2/3}Tb_{1/3})_2AlC$

Figure 6(a) shows the refined neutron diffraction data obtained at 50 K without an applied magnetic field. The refined crystal structure is consistent with previous results [15]. Two regions $Q = 3.08$–3.14 Å^{-1} and $Q = 4.36$–4.43 Å^{-1} are not shown to exclude the strong peaks of the textured Al sample holder. The refined parameters at 50 K are used as input for the low temperature refinement. Figure 6(b) shows the magnetic scattering at 5 K with an applied magnetic field of 6 T. The nuclear contribution is subtracted by using the pattern shown in figure 6(a). The major peak in figure 6(b) can be indexed with $\boldsymbol{k_1} =$ (0, 2/3, 0). The remaining peaks can be indexed with $\boldsymbol{k_2} =$ (0, 0, 0) and $\boldsymbol{k_3} = (0, 1/2, 0)$, where $\boldsymbol{k_3}$ corresponds to the zero field magnetic structure.

The symmetry consideration for $\boldsymbol{k} = (0\ \delta\ 0)$ within the *C*2/*c* space group is the same for $\boldsymbol{k_1}$ ($\delta = 2/3$) and $\boldsymbol{k_3}$ ($\delta = 1/2$). It decomposes into two irreducible representations. $\boldsymbol{k_2} = (0, 0, 0)$ decomposes into four irreducible representations. The symmetry analysis is provided in table 2 of appendix, where the representation Γ and basis vectors φ are defined.

We considered all models which are allowed by symmetry. The $\boldsymbol{k_3}$ structure is identical to the zero field structure [15],

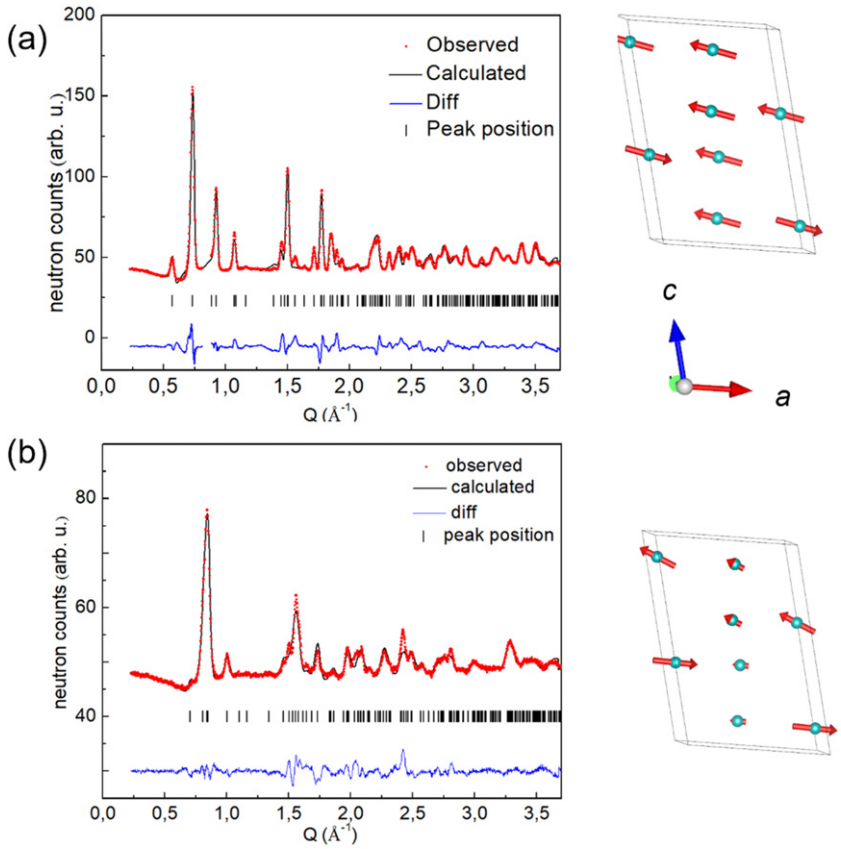

Figure 5. Zero field magnetic scattering for $(Mo_{2/3}Dy_{1/3})_2AlC$. (a) Magnetic scattering at 1.5 K. (b) Magnetic scattering at 14 K. The nuclear scattering was subtracted by data measured at 18 K.

being not fully suppressed by the applied magnetic field. The $\boldsymbol{k_2}$ structure can be well fitted with a single irreducible representations Γ_3, corresponding to a ferromagnetic structure along the a-axis. Other models can be excluded by comparing with the obtained data, for example, Γ_2 would lead to a strong (100) peak at $Q = 0.46$ Å^{-1}, which is not observed. We also considered Γ_1. The best agreement was achieved with the basis vector φ_2 and φ_3 of Γ_1 with an agreement factor of $\boldsymbol{R}_{\rm mag} = 60\%$. However, Γ_1 fails to reproduce the intensity; for example, the most intense (001) peak cannot be accounted for by Γ_1. Thus, Γ_1 can be discarded.

In the following, we turn to the $\boldsymbol{k_1}$ structure. The best agreement was achieved with the basis vector φ_1 and φ_3 of Γ_2, with agreement factor $\boldsymbol{R}_{\rm mag} = 18\%$. φ_1 corresponds to F_x modes, while φ_3 corresponds to F_z modes, in Bertaut's notation. In the refined structure, the magnetic moments are confined in the a–c plane. The magnetic moments are arranged in an up–up–down configuration, where the moment size is 4.7 μ_B and 9.4 μ_B, respectively.

As the highest field in the current experiment setup is 6 T, we could reach the first magnetization plateau of $(Mo_{2/3}Tb_{1/3})_2AlC$. We did another scan in an applied field of 4.7 T (not shown), though no significant difference can be observed in a comparison with the scan in a field of 6 T. This suggests that the magnetic configuration is robust within the magnetization plateau.

Figure 6(c) shows the magnetic scattering at 22 K in 6 T. $(Mo_{2/3}Tb_{1/3})_2AlC$ orders in an incommensurate spin density wave structure at this temperature in zero field. As shown in figure 6(c), the field induced structure is similar to that of the 5 K one. The magnetic scattering can be well fitted with $\boldsymbol{k_1} = (0, 2/3, 0)$ and $\boldsymbol{k_2} = (0, 0, 0)$. Further increasing the temperature, the magnetic reflections corresponding to $\boldsymbol{k_1}$ disappears while magnetic reflections corresponding to $\boldsymbol{k_2}$ can be seen clearly up to 50 K.

4.2. Field induced magnetic structure of $(Mo_{2/3}Dy_{1/3})_2AlC$

The magnetic behavior of $(Mo_{2/3}Dy_{1/3})_2AlC$ is similar to that of $(Mo_{2/3}Tb_{1/3})_2AlC$. Both show two successive transitions and multiple magnetization plateaus. However, the critical field is smaller in $(Mo_{2/3}Dy_{1/3})_2AlC$, see figure 3. Three field induced transitions are found below 6 T. The low critical field allows us to probe different magnetization plateaus with neutron diffraction in a magnetic field.

Figure 7(a) shows the magnetic scattering of $(Mo_{2/3}Dy_{1/3})_2AlC$ recorded at different field. Each field is chosen to represent a magnetization plateau phase. The pattern can be fitted with two propagation vectors, $\boldsymbol{k_1} = (0, 2/3, 0)$, $\boldsymbol{k_2} = (0, 0, 0)$. Similar to $(Mo_{2/3}Tb_{1/3})_2AlC$, we considered each component separately. $\boldsymbol{k_2} = (0, 0, 0)$ corresponds to a ferromagnetic arrangement along the a axis. $\boldsymbol{k_1} = (0, 2/3, 0)$ is antiferromagnetic along a axis; it consists of two 1/2**m** up spins and one **m** down spin. Figure 7(b) shows the

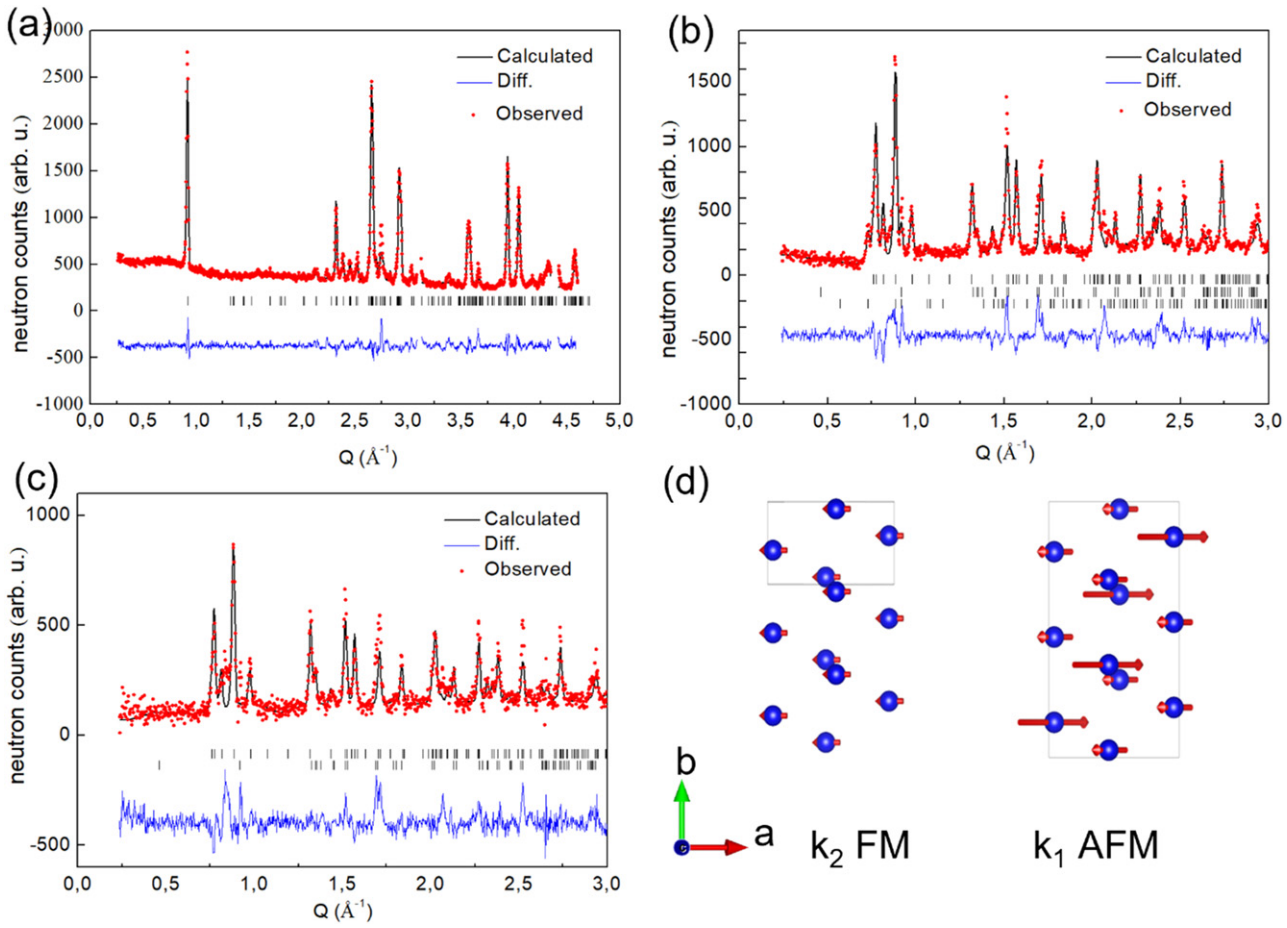

Figure 6. Magnetic scattering analysis for $(Mo_{2/3}Tb_{1/3})_2AlC$. (a) Neutron diffraction at 50 K, zero field. Two intense peaks from the Al sample holder are excluded. (b) Magnetic scattering at 5 K in 6 T magnetic field. The nuclear scattering was subtracted by the data in (a). (c) Magnetic scattering at 22 K in 6 T magnetic field. (d) Schematic magnetic structure.

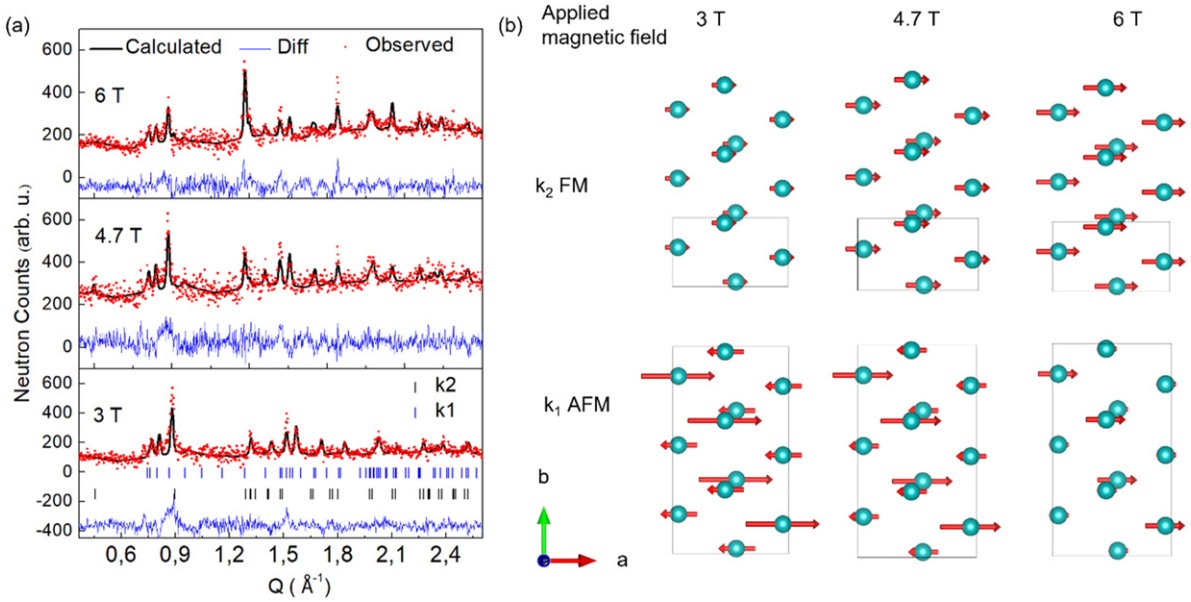

Figure 7. Magnetic scattering analysis for $(Mo_{2/3}Dy_{1/3})_2AlC$ in an applied magnetic field. (a) Magnetic scattering at 5 K in 3 T, 4.7 T, and 6 T. Each field corresponds to a magnetic phase. The nuclear scattering was subtracted using the pattern at 20 K. (b) Schematic evolution of magnetic structure (blue dots indicate the positions of Dy) with applied magnetic field. The squares denote the size of the magnetic unit cell. The length of the arrows scale with the magnetic moment.

Table 1. Basis vectors of the irreducible representations for the little group of $\boldsymbol{k} = (0, \delta, 0)$ within the $C2/c$ space group. A little group is a subgroup that is compatible with the magnetic translation symmetry.

Orbit 1			
Representation	Basis vector	1 (x, y, z)	2 $(-x, y, -z + 1/2)$
Γ_1	φ_1	[1, 0, 0]	[−1, 0, 0]
	φ_2	[0, 1, 0]	[0, 1, 0]
	φ_3	[0, 0, 1]	[0, 0, −1]
Γ_2	φ_1	[1, 0, 0]	[1, 0, 0]
	φ_2	[0, 1, 0]	[0, −1, 0]
	φ_3	[0, 0, 1]	[0, 0, 1]
Orbit 2			
Representation	Basis vector	−1 $(-x, -y, -z)$	c $(x, -y, z + 1/2)$
Γ_1	φ_1	[1, 0, 0]	[−1, 0, 0]
	φ_2	[0, 1, 0]	[0, 1, 0]
	φ_3	[0, 0, 1]	[0, 0, −1]
Γ_2	φ_1	[1, 0, 0]	[1, 0, 0]
	φ_2	[0, 1, 0]	[0, −1, 0]
	φ_3	[0, 0, 1]	[0, 0, 1]

Table 2. Irreducible representations of the little group of $\mathbf{k} = (0, 0, 0)$ within the $C2/c$ space group.

Representation	Basis vector	1 (x, y, z)	2 $(-x, y, -z + 1/2)$	−1 $(-x, -y, -z)$	c $(x, -y, z + 1/2)$
Γ_1	φ_1 G_x	[1, 0, 0]	[−1, 0, 0]	[1, 0, 0]	[−1, 0, 0]
	φ_2 F_y	[0, 1, 0]	[0, 1, 0]	[0, 1, 0]	[0, 1, 0]
	φ_3 G_z	[0, 0, 1]	[0, 0, −1]	[0, 0, 1]	[0, 0, −1]
Γ_2	φ_4 F_x	[1, 0, 0]	[1, 0, 0]	[1, 0, 0]	[1, 0, 0]
	φ_1 G_y	[0, 1, 0]	[0, −1, 0]	[0, 1, 0]	[0, −1, 0]
	φ_2 F_z	[0, 0, 1]	[0, 0, 1]	[0, 0, 1]	[0, 0, 1]
Γ_3	φ_1 A_x	[1, 0, 0]	[−1, 0, 0]	[−1, 0, 0]	[1, 0, 0]
	φ_2 C_y	[0, 1, 0]	[0, 1, 0]	[0, −1, 0]	[0, −1, 0]
	φ_3 A_z	[0, 0, 1]	[0, 0, −1]	[0, 0, −1]	[0, 0, 1]
Γ_4	φ_4 C_x	[1, 0, 0]	[1, 0, 0]	[−1, 0, 0]	[−1, 0, 0]
	φ_1 A_y	[0, 1, 0]	[0, −1, 0]	[0, −1, 0]	[0, 1, 0]
	φ_2 C_z	[0, 0, 1]	[0, 0, 1]	[0, 0, −1]	[0, 0, −1]

schematic spin configurations in the a–b plane at different magnetic field. The magnitude of the AFM component $\boldsymbol{k_1}$ decreases with magnetic field, while the FM component $\boldsymbol{k_2}$ increases.

Magnetization plateaus have been observed in various materials, such as in TbB_4 with Shastry–Sutherland lattice [20], Kagomeé Lattice $SrCo_6O_{11}$ [24], triangular lattice $CoNb_2O_6$ [25], etc. Different mechanisms have been proposed. For example, it is suggested that magnetization plateau in TbB_4 arise from a combined effect of magnetic frustration and quadrupole interaction [19]. In our recent muon spin rotation study, both dipolar interaction and RKKY interaction play a role in the observed short-range order and spin fluctuation [21]. In addition, both $(Mo_{2/3}Dy_{1/3})_2AlC$ and $(Mo_{2/3}Tb_{1/3})_2AlC$ show easy plane anisotropy. We suggest that the rich magnetic phase diagram is result of competing interaction in the presence of magnetocrystalline anisotropy.

In conclusion, we determined the magnetic field–temperature phase diagram of the spin textures in $(Mo_{2/3}Dy_{1/3})_2AlC$ and $(Mo_{2/3}Tb_{1/3})_2AlC$. Similar to $(Mo_{2/3}Tb_{1/3})_2AlC$, in zero field $(Mo_{2/3}Dy_{1/3})_2AlC$ forms a spin density wave at 16 K in zero magnetic field, and orders antiferromagnetically at 13 K. We also studied the magnetization plateaus with neutron diffraction in applied magnetic field. Ferromagnetic component with $\boldsymbol{k} = (0, 0, 0)$ and antiferromagnetic components with $\boldsymbol{k} = (0, 2/3, 0)$ coexist in the field induced phases. We suggested that the rich phase diagram may be a result of competing ferro- and antiferromagnetic correlation in the presence of magnetocrystalline anisotropy. Neutron scattering on single crystal is underway. By improving the understanding of the magnetic phase diagram in $(Mo_{2/3}Dy_{1/3})_2AlC$ and $(Mo_{2/3}Tb_{1/3})_2AlC$, we have at least in part clarified the competition between ferromagnetic and antiferromagnetic correlations, which is important for understanding these magnetic laminates, and potentially magnetic MAX phases in general.

Acknowledgments

J R acknowledge support from the Knut and Alice Wallenberg (KAW) Foundation for a Fellowship/Scholar Grant and Project funding (KAW 2020.0033). This work was also financially supported by the Deutsche Forschungsgemeinschaft (DFG) within CRC/TRR 270, project B02 (Project-ID 405553726), by the Flag-ERA JTC 2017 project entitled 'MORE-MXenes', and by the ANR project referenced ANR-18-CE09-0041. M F acknowledges co-funding by the government of the Russian Federation (Agreement No. 075-15-2019-1886). Helpful discussions with Claire Colin are thankfully acknowledged.

Data availability statement

The data that support the findings of this study are available upon reasonable request from the authors.

Appendix

See tables 1 and 2.

ORCID iDs

Quanzheng Tao https://orcid.org/0000-0002-4073-5242
Clemens Ritter https://orcid.org/0000-0003-3674-3378
Rose-Marie Galera https://orcid.org/0000-0003-4566-1841

References

[1] Sokol M, Natu V, Kota S and Barsoum M W 2019 On the chemical diversity of the MAX phases *Trends Chem.* **1** 210–23
[2] Barsoum M W 2013 *MAX Phases: Properties of Machinable Ternary Carbides and Nitrides* (New York: Wiley)
[3] Fashandi H *et al* 2017 Synthesis of Ti_3AuC_2, $Ti_3Au_2C_2$ and Ti_3IrC_2 by noble metal substitution reaction in Ti_3SiC_2 for high-temperature-stable Ohmic contacts to SiC *Nat. Mater.* **16** 814–8
[4] Naguib M, Kurtoglu M, Presser V, Lu J, Niu J, Heon M, Hultman L, Gogotsi Y and Barsoum M W 2011 Two-dimensional nanocrystals produced by exfoliation of Ti_3AlC_2 *Adv. Mater.* **23** 4248–53
[5] VahidMohammadi A, Rosen J and Gogotsi Y 2021 The world of two-dimensional carbides and nitrides (MXenes) *Science* **372** abf1581
[6] Huang B *et al* 2017 Layer-dependent ferromagnetism in a van der Waals crystal down to the monolayer limit *Nature* **546** 270–3
[7] Gong C *et al* 2017 Discovery of intrinsic ferromagnetism in two-dimensional van der Waals crystals *Nature* **546** 265–9
[8] Ingason A S *et al* 2013 Magnetic self-organized atomic laminate from first principles and thin film synthesis *Phys. Rev. Lett.* **110** 195502
[9] Ingason A S *et al* 2014 A nanolaminated magnetic phase: Mn_2GaC *Mater. Res. Lett.* **2** 89–93
[10] Ingason A S, Pálsson G K, Dahlqvist M and Rosén J 2016 Long-range antiferromagnetic order in epitaxial Mn_2GaC thin films from neutron reflectometry *Phys. Rev.* B **94** 024416
[11] Ingason A S, Dahlqvist M and Rosen J 2016 Magnetic MAX phases from theory and experiments; a review *J. Phys.: Condens. Matter* **28** 433003
[12] Tao Q *et al* 2017 Two-dimensional $Mo_{1.33}C$ MXene with divacancy ordering prepared from parent 3D laminate with in-plane chemical ordering *Nat. Commun.* **8** 14949
[13] Meshkian R *et al* 2018 W-based atomic laminates and their 2D derivative $W_{1.33}C$ MXene with vacancy ordering *Adv. Mater.* **30** 1706409
[14] Persson I *et al* 2018 Tailoring structure, composition, and energy storage properties of MXenes from selective etching of in-plane, chemically ordered MAX phases *Small* **14** 1703676
[15] Tao Q *et al* 2019 Atomically layered and ordered rare-earth *i*-MAX phases: a new class of magnetic quaternary compounds *Chem. Mater.* **31** 2476–85
[16] Champagne A *et al* 2019 First-order Raman scattering of rare-earth containing *i*-MAX single crystals $(Mo_{2/3}RE_{1/3})_2AlC$ (RE = Nd, Gd, Dy, Ho, Er) *Phys. Rev. Mater.* **3** 053609
[17] Petruhins A, Lu J, Hultman L and Rosen J 2019 Synthesis of atomically layered and chemically ordered rare-earth (RE) *i*-MAX phases; $(Mo_{2/3}RE_{1/3})_2GaC$ with RE = Gd, Tb, Dy, Ho, Er, Tm, Yb, and Lu *Mater. Res. Lett.* **7** 446–52
[18] Yang J, Liu R, Jia N, Wu K, Fu X, Wang Q and Cui W 2021 Novel W-based in-plane chemically ordered $(W_{2/3}R_{1/3})_2AlC$ (R = Gd, Tb, Dy, Ho, Er, Tm and Lu) MAX phases and their 2D $W_{1.33}C$ MXene derivatives *Carbon* **183** 76–83
[19] Yoshii S, Yamamoto T, Hagiwara M, Michimura S, Shigekawa A, Iga F, Takabatake T and Kindo K 2008 Multistep magnetization plateaus in the Shastry–Sutherland system TbB_4 *Phys. Rev. Lett.* **101** 087202
[20] Yoshii S *et al* 2009 Neutron diffraction study on the multiple magnetization plateaus in TbB_4 under pulsed high magnetic field *Phys. Rev. Lett.* **103** 077203
[21] Potashnikov D *et al* 2021 Magnetic structure determination of high-moment rare-earth-based laminates *Phys. Rev.* B **104** 174440
[22] Ouisse T, Sarigiannidou E, Chaix-Pluchery O, Roussel H, Doisneau B and Chaussende D 2013 High temperature solution growth and characterization of Cr_2AlC single crystals *J. Cryst. Growth* **384** 88–95
[23] Rodriguez-Carvajal J 1993 Recent advances in magnetic structure determination by neutron powder diffraction *Phys. Rev. B Condens. Matter* **192** 55–69
[24] Matsuda T *et al* 2015 Observation of a devil's staircase in the novel spin-valve system $SrCo_6O_{11}$ *Phys. Rev. Lett.* **114** 236403
[25] Kobayashi S, Mitsuda S, Hosaka S, Tamatsukuri H, Nakajima T, Koorikawa H, Prokeš K and Kiefer K 2016 Neutron diffraction study of low-temperature magnetic phase diagram of an isosceles-triangular-lattice Ising antiferromagnet $CoNb_2O_6$ *Phys. Rev.* B **94** 134427